



Cite this: *Nanoscale Adv.*, 2022, **4**, 4358

An inorganic–organic hybrid nanomaterial with a core–shell structure constructed by using Mn–BTC and Ag₅[BW₁₂O₄₀] for supercapacitors and photocatalytic dye degradation†

Caihong Shi,^a Ning Kang,^a Chunmei Wang,^a Kai Yu, ^{a,b} Jinghua Lv,^a Chunxiao Wang^a and Baibin Zhou ^{a,b}

Creating inorganic–organic hybrids with polyoxometalates (POMs) and metal–organic frameworks (MOFs) as energy storage and dye-degradation materials remains challenging. Here, a new hybrid nanomaterial Mn–BTC@Ag₅[BW₁₂O₄₀] is synthesized by using Ag₅[BW₁₂O₄₀] and Mn₃(BTC)₂(H₂O)₆ (Mn–BTC, BTC = 1,3,5-benzenetricarboxylic acid) through a plain grinding method. The structure and morphology characterization by scanning electron microscopy (SEM), powder X-ray diffraction (XRD), and transmission electron microscopy (TEM) shows that the synthetic products have core–shell construction. Due to its unique structure wherein the core is Mn–BTC and the shell is Ag₅[BW₁₂O₄₀], it exhibits excellent capacitance performance. In a three-electrode system where nickel foam is a collector, at a current density of 1 A g⁻¹, its specific capacitance is 198.09 F g⁻¹; after 5000 cycles, the capacitance retention rate is 94.4%. When the power density is 503.1 W kg⁻¹, the symmetrical supercapacitor reveals a high energy density which is 10.9 W h kg⁻¹. At the same time, the capacitance retention is 92.9% after 5000 cycles which showed good cycle stability. The photocatalytic degradation efficiencies of rhodamine B (RhB), methyl orange (MO) and methylene blue (MB) dyes exceed 90% after 140 min, and the degradation results remained unchanged after five photocatalytic cycles. The photocatalytic degradation mechanism shows that ·OH has a major effect. The results show that this research provides a fresh idea for the development of energy storage and dye photocatalytic degradation materials.

Received 3rd August 2022
Accepted 1st September 2022

DOI: 10.1039/d2na00510g
rsc.li/nanoscale-advances

1. Introduction

With the development of science and technology, the shortage of energy and environmental pollution have become a severe problem for mankind.¹ Therefore, the development and utilization of renewable clean energy and the design of efficient energy storage equipment need to be researched.^{2–4} As a kind of energy storage device with high specific capacitance and long cycle lifetime, supercapacitors have attracted extensive attention from scholars.^{5–8} The design and synthesis of high-performance electrode materials are key factors in the development of supercapacitors. However, traditional materials invariably have certain shortcomings, for example, a poor environmental protection effect and low price–performance ratio.⁹ Therefore,

the exploitation of new electrode materials with high capacitance performance and environmental protection plays an important role in the development of supercapacitors.

Polyoxometalates (POMs) are discrete, polynucleated metal–oxygen cluster compounds formed by transition metals in a high oxidation state, with a variety of structures and size and good electron transport capacity.^{10–16} Because of their acidity, invertible redox activity, thermal stability, high charge density and electron storage capacity, POMs have broad prospects in the application of supercapacitors.^{17–20} The Keggin type is the most widely studied type of POMs.^{21–24} Due to its excellent structural stability and easy modification, Keggin-type POMs can play different roles in the design and synthesis of peculiar structural compounds. Compared with other POMs, [BW₁₂O₄₀]^{5–}{(BW₁₂)} has a high surface charge density and is more likely to have a mutual effect with transition metals, which is conducive to the formation of more complexes. Therefore, the synthesis and properties of inorganic–organic hybrids based on {BW₁₂} have a good prospect. In recent years, scientists have used d-zone transition metals to synthesize many catalysts with excellent performance, among which Co, Ni, Cu and Mn have attracted extensive attention.^{25–31} According to reports in the

^aKey Laboratory for Photonic and Electronic Bandgap Materials, Ministry of Education, Harbin Normal University, Harbin, Heilongjiang 150025, China. E-mail: hlyukai188@163.com; zhou_bai_bin@163.com

^bKey Laboratory of Synthesis of Functional Materials and Green Catalysis, Colleges of Heilongjiang Province, Harbin Normal University, Harbin, Heilongjiang 150025, China

† Electronic supplementary information (ESI) available. See <https://doi.org/10.1039/d2na00510g>



literature,^{32–35} $\{BW_{12}\}$ hybrids are mostly synthesized by the hydrothermal method and are diffusely accustomed in electrocatalysis, photocatalysis and other fields. However, the electrode materials used as supercapacitors are less frequently reported.^{36,37} At the same time, the reaction conditions of the hydrothermal method are difficult to control, with low yield and poor reproducibility, which hinders its large-scale application. Therefore, it is still challenging to explore a more convenient method for the preparation of high capacitive POMs. To resolve this question, we designed POMs fixed on metal-organic frameworks (MOFs) by a solution or grinding method^{38–44} and prepared a POM-based hybrid that showed good stability in the water environment while maintaining its excellent electrochemical behavior. Because the grinding method is a fast and effective synthesis strategy, it has the advantages of simple operation, high yield and controllable reaction conditions.^{45–49} By introducing MOFs into a Keggin-type system to obtain polyoxometalate-based metal-organic frameworks (POMOFs) with a novel structure and excellent performance, the performance of such compounds can be improved.^{50,51}

Based on the above study, we applied Keggin type $[BW_{12}O_{40}]^{5-}$, Mn^{2+} and a H_3BTC ligand to prepare the $Mn-BTC@Ag_5[BW_{12}O_{40}]$ nanomaterial by the grinding method. At the same time, $Ag_5[BW_{12}O_{40}]$, Mn-BTC, and $Mn-BTC@Ag_5[BW_{12}O_{40}]$ were used as the electrode materials of supercapacitors, and their electrochemical properties were studied. In addition, with $Mn-BTC@Ag_5[BW_{12}O_{40}]$ as a catalyst, the photocatalytic degradation of rhodamine B (RhB), methyl orange (MO) and methylene blue (MB) dyes was investigated.

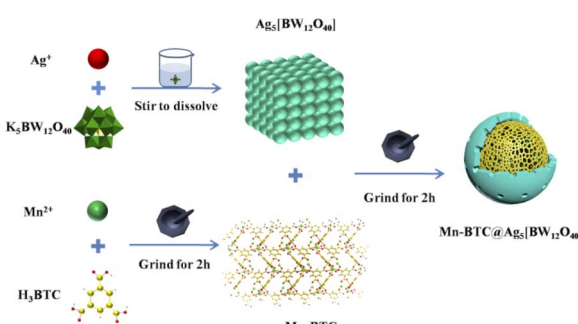
2. Experimental section

2.1. Synthesis of Mn-BTC

H_3BTC (0.1400 g, 0.6667 mmol) and $Mn(NO_3)_2 \cdot 6H_2O$ (0.2400 g, 0.8361 mmol) were ground in an agate mortar for 2 h, gradually becoming a light pink color, and then scoured with ethanol and distilled water. The pale pink powder sample of Mn-BTC was procured after drying for 1 day at 60 °C.

2.2. Synthesis of $Mn-BTC@Ag_5[BW_{12}O_{40}]$

Mn-BTC (0.2651 g, 1 mmol) and $Ag_5[BW_{12}O_{40}]$ (1.6981 g, 0.5 mmol, its synthesis is provided in the ESI†) were ground in an



Scheme 1 The synthesis strategy of the $Mn-BTC@Ag_5[BW_{12}O_{40}]$ nanomaterial.

agate mortar for 2 h, and the pale grey powdery sample $Mn-BTC@Ag_5[BW_{12}O_{40}]$ was procured and then scoured with ethanol and distilled water. In the end, the sample was dried for 1 day at 60 °C. The synthesis strategy of $Mn-BTC@Ag_5[BW_{12}O_{40}]$ is shown in Scheme 1.

3. Results and discussion

3.1. Characterization

As can be seen from Fig. 1a, the IR spectra of $Mn-BTC@Ag_5[BW_{12}O_{40}]$, $Ag_5[BW_{12}O_{40}]$, and Mn-BTC show that the peak at 3430–3500 cm^{-1} is deemed as the typical vibration of water molecules. And characteristic bands of $Ag_5[BW_{12}O_{40}]$ appearing at 958.6, 917.1, 833.6, and 756.1 cm^{-1} correspond to the stretching vibrations of $\nu(W-O_d)$, $\nu(B-O_a)$, $\nu(W-O_b-W)$, and $\nu(W-O_c-W)$ of $[BW_{12}O_{40}]^{5-}$.^{52,53} The peak is slightly shifted compared with those reported in the literature,⁵⁴ which is due to the interaction between $[BW_{12}O_{40}]^{5-}$ and Ag^+ , indicating the successful synthesis of $Ag_5[BW_{12}O_{40}]$. The 1720.4, 1610.5, 1454.2, 1404.1 and 1278.7 cm^{-1} characteristic peaks of Mn-BTC belong to the characteristic bands of $C=O$, the benzene ring and $C-O$ of BTC^{3-} .⁵⁵ However, the band was slightly shifted when compared to that of the free H_3BTC ligand.⁵⁵ This indicates that H_3BTC and Mn^{2+} coordinate to form Mn-BTC, similar to that in the literature.⁵⁶ In the IR spectrum of $Mn-BTC@Ag_5[BW_{12}O_{40}]$, 956.6, 917.1, 833.6, and 756.1 cm^{-1} are characteristic peaks of the $[BW_{12}O_{40}]^{5-}$ cluster and show that $Ag_5[BW_{12}O_{40}]$ maintained its original Keggin structure in $Mn-BTC@Ag_5[BW_{12}O_{40}]$. The vibrations at 1404.1 and 1720.5 cm^{-1} correspond to the carboxyl vibration band of the BTC^{3-} ligand, and the vibrations at 1610.5, 1454.2, and 1278.7 cm^{-1} correspond to the typical peaks of the benzene ring of the BTC ligand, indicating the successful synthesis of the nanomaterial. Relative to $Ag_5[BW_{12}O_{40}]$, the IR spectrum of $Mn-BTC@Ag_5[BW_{12}O_{40}]$ shows a mild variation, where the $W-O_d$ spectrum moves 2 cm^{-1} , possibly because of the synergistic effect between $Ag_5[BW_{12}O_{40}]$ with Mn-BTC, which proves the successful synthesis of $Mn-BTC@Ag_5[BW_{12}O_{40}]$.

Fig. 1b shows the XRD patterns of $Ag_5[BW_{12}O_{40}]$, Mn-BTC, and $Mn-BTC@Ag_5[BW_{12}O_{40}]$. The diffraction peaks of the synthesized $Ag_5[BW_{12}O_{40}]^{40}$ and $Mn_3(BTC)_2(H_2O)_6$ (Mn-BTC)⁴¹ are consistent with the previously reported results, indicating that $Ag_5[BW_{12}O_{40}]$ and Mn-BTC are synthesized. As can be seen from the figure, the crystallinity of $Mn-BTC@Ag_5[BW_{12}O_{40}]$ is not high enough, but the main diffraction is the same as that for

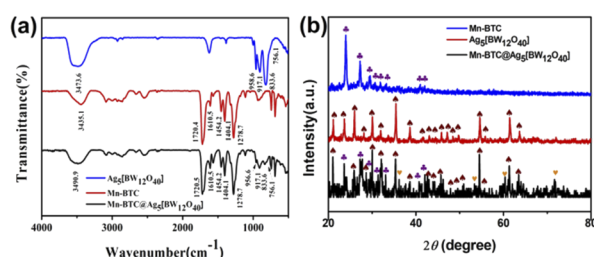


Fig. 1 (a) IR spectra and (b) XRD spectra.



$\text{Ag}_5[\text{BW}_{12}\text{O}_{40}]$ and Mn-BTC. This indicates that $\text{Ag}_5[\text{BW}_{12}\text{O}_{40}]$ and Mn-BTC are still retained in the new nanomaterial. In the meantime, the relative intensity of the diffraction peak of Mn-BTC@ $\text{Ag}_5[\text{BW}_{12}\text{O}_{40}]$ is more consistent with that of $\text{Ag}_5[\text{BW}_{12}\text{O}_{40}]$, so this can prove that the compound is a core-shell structure of Mn-BTC encapsulated in $\text{Ag}_5[\text{BW}_{12}\text{O}_{40}]$. Besides, the synthesized Mn-BTC@ $\text{Ag}_5[\text{BW}_{12}\text{O}_{40}]$ has four new diffraction peaks with angles (2θ) of 36.16° , 53.36° , 60.38° , and 71.66° (see Fig. 1b \heartsuit identification), which can be attributed to the coordination effect between $\text{Ag}_5[\text{BW}_{12}\text{O}_{40}]$ ions with Mn-BTC, proving the synthesis of the target complex.

Fig. S1† shows the thermogravimetric (TG) curve of Mn-BTC@ $\text{Ag}_5[\text{BW}_{12}\text{O}_{40}]$. As can be seen from the figure, Mn-BTC@ $\text{Ag}_5[\text{BW}_{12}\text{O}_{40}]$ involves two-step weightlessness steps. The first weight loss of 1.81% at 100°C indicates that the compound has lost water molecules on its surface. The decomposition of the compound in the range of $260\text{--}550^\circ\text{C}$ is the second weightlessness process, and the weightlessness rate is 17.94%. The final calcination results in tungsten carbide, silver and manganese oxide, are consistent with the literature.^{40,41} The actual weight loss obtained through TG is consistent with the calculated theoretical weight loss, and the resulting substance is the target compound.

From Fig. 2, the morphology of Mn-BTC@ $\text{Ag}_5[\text{BW}_{12}\text{O}_{40}]$ was further characterized through SEM, and the elemental composition and content were also tested by EDS and EDX. Among them, the structure of Mn-MOF has the morphology of long nanorods,⁵⁶ $\text{Ag}_5[\text{BW}_{12}\text{O}_{40}]$ is a cube⁴⁰ and the morphology of Mn-BTC@ $\text{Ag}_5[\text{BW}_{12}\text{O}_{40}]$ is a long and thin rod, so it can be inferred that the compound is a core-shell structure in which $\text{Ag}_5[\text{BW}_{12}\text{O}_{40}]$ is attached to the surface of Mn-BTC, with Mn-BTC as the core and $\text{Ag}_5[\text{BW}_{12}\text{O}_{40}]$ as the shell (see Fig. 2a), and the core-shell structure is more likely to afford favourable attachment points for making the reaction more likely to proceed smoothly. The EDS (Fig. 2b) and EDX (Fig. S2a–g†) tests of Mn-BTC@ $\text{Ag}_5[\text{BW}_{12}\text{O}_{40}]$ showed the presence and uniform distribution of the elements B, W, C, O, Ag and Mn.

Fig. 2c shows the TEM image of Mn-BTC@ $\text{Ag}_5[\text{BW}_{12}\text{O}_{40}]$, which further shows the morphology of the core-shell structure. HRTEM was used to further illustrate the relationship between

Mn-BTC and $\text{Ag}_5[\text{BW}_{12}\text{O}_{40}]$, as shown in Fig. 2d. As can be seen from the figure which shows the Mn-BTC@ $\text{Ag}_5[\text{BW}_{12}\text{O}_{40}]$ nanomaterial, the crystal plane fringe spacings of Mn-BTC and $\text{Ag}_5[\text{BW}_{12}\text{O}_{40}]$ are 0.382 nm and 0.256 nm, respectively. In addition, there are lots of micropores with diameters of about 1–3 nm in the Mn-BTC@ $\text{Ag}_5[\text{BW}_{12}\text{O}_{40}]$ composite (marked by red arrows in Fig. 2d). The observations prove that $\text{Ag}_5[\text{BW}_{12}\text{O}_{40}]$ can be covered on the Mn-BTC face, which is in accord with SEM observations.

Fig. S3† shows the N_2 absorption isotherm of Mn-BTC@ $\text{Ag}_5[\text{BW}_{12}\text{O}_{40}]$, and it shows a typical IV-type isotherm for a mesoporous structure. A mesoporous hysteresis loop was observed in the adsorption curve due to the pore structure between the particles. The BET surface area and average desorption pore sizes are $12.54\text{ m}^2\text{ g}^{-1}$ and 8.72 nm for Mn-BTC@ $\text{Ag}_5[\text{BW}_{12}\text{O}_{40}]$, greater than those of Mn-BTC ($8.86\text{ m}^2\text{ g}^{-1}$; 5.86 nm)⁴¹ and $\text{Ag}_5[\text{BW}_{12}\text{O}_{40}]$ ($8.26\text{ m}^2\text{ g}^{-1}$; 1.92 nm)⁴⁰ (measured by the BJH method) (Fig. S4†). The above data indicate that the adhesion of $\text{Ag}_5[\text{BW}_{12}\text{O}_{40}]$ to the Mn-BTC surface improves the porosity of Mn-BTC@ $\text{Ag}_5[\text{BW}_{12}\text{O}_{40}]$.

Furthermore, XPS measurements were performed to analyze the composition and elemental valence states for Mn-BTC@ $\text{Ag}_5[\text{BW}_{12}\text{O}_{40}]$. By analyzing the B spectrum (Fig. 3a), the typical peak of B–O is 193.8 eV, and the peak at 192.2 eV is B 1 s, indicating the existence of B^{3+} .⁵⁷ As can be seen from Fig. 3b, the W 4f energy spectrum has prominent peaks at 35.4 and 33.2 eV, designated to W 4f_{7/2} and W 4f_{5/2} of W^{6+} .^{58–60} It conforms to the typical electronic states of polytungstate. In Fig. 3c, the high-resolution O 1s spectrum has an obvious peak at 529.4 eV, which is due to Ag–O binding energy.⁶¹ Fig. 3d shows the XPS spectrum of the resolved C 1s with two peaks at 282.6 eV and 286.7 eV, belonging to the C–O, C=O groups in the H_3BTC ligand.⁵⁵ Fig. 3e shows that Ag 3d has two main peaks of 366.1 and 372.1 eV, designated to Ag 3d_{5/2} and Ag 3d_{3/2} of Ag^+ .^{62,63} What's more, the XPS survey scan of Mn in Fig. 3f shows that three peaks at 632.6, 640 and 658.9 eV correspond to Mn 2p_{3/2}, Mn–O and Mn 2p_{1/2}, which proves the existence of Mn^{2+} .⁶⁴ Fig. S5† shows the XPS full spectra of Mn-BTC@ $\text{Ag}_5[\text{BW}_{12}\text{O}_{40}]$, which proves the coexistence of C, O, B, W, Ag and Mn elements; its content is similar to the molecular formula and is consistent with the EDS (Fig. 2b) results. All the above indicate that Mn-BTC@ $\text{Ag}_5[\text{BW}_{12}\text{O}_{40}]$ was successfully synthesized.

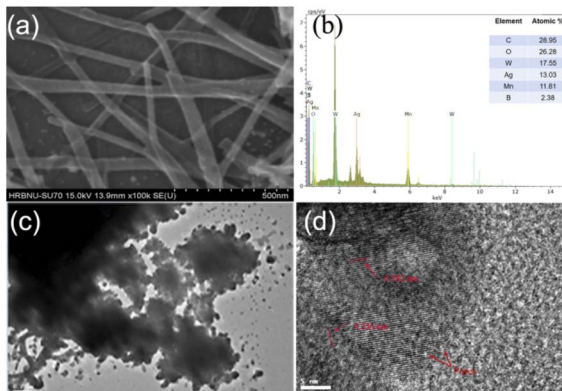


Fig. 2 (a) SEM image, (b) EDS, (c) TEM image and (d) HRTEM image of Mn-BTC@ $\text{Ag}_5[\text{BW}_{12}\text{O}_{40}]$.

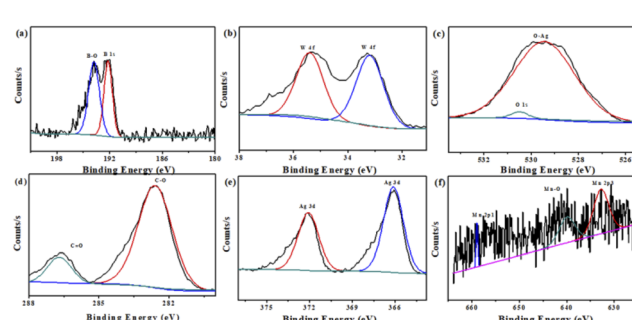


Fig. 3 XPS spectra of (a) B 1s, (b) W 4f, (c) O 1s, (d) C 1s, (e) Ag 3d and (f) Mn 2p for the nanomaterial.



3.2. Electrochemical performance

The three prepared electrodes of Mn-BTC@Ag₅[BW₁₂O₄₀]-NF, Ag₅[BW₁₂O₄₀]-NF and Mn-BTC-NF were subjected to three-electrode CV and GCD tests in 1 M Na₂SO₄. The voltage window and scan rates of CV measurements are respectively from -0.5 V to 0.6 V and from 5 mV s⁻¹ to 100 mV s⁻¹. As can be seen from Fig. 4a, the CV curve at a scanning speed of 50 mV s⁻¹, an oxidation peak and both reduction peaks were observed at Ag₅[BW₁₂O₄₀]-NF, which could be ascribed to a redox process for W⁶⁵ and a reduction peak for Ag⁺.⁶⁶ Mn-BTC could not show the redox peak,⁵⁶ so it can be proved that two oxidation peaks and three reduction peaks of Mn-BTC@Ag₅[BW₁₂O₄₀]-NF were caused by Ag₅[BW₁₂O₄₀], which further proves that the synthesized compound is the target compound. For Mn-BTC@Ag₅[BW₁₂O₄₀]-NF, there are two pairs of invertible redox peaks I-I' and II-II' with average peak potentials $E_{1/2} = (E_{pa} + E_{pc})/2$ at +189.9 and +42.3 mV, respectively, corresponding to single-electron procedures at the W of [BW₁₂O₄₀]⁵ (ref. 65) (reaction (a)) and Mn²⁺ (ref. 66) (reaction (b)), respectively. This may be because after coordination with Ag₅[BW₁₂O₄₀], Mn-BTC exhibited reversible redox peaks, which may have originated from the reversible valence state changes of Mn ions.⁶⁶ The Mn-BTC@Ag₅[BW₁₂O₄₀]-NF electrode also has one reduction peak III' of potential -234.6 mV, which is considered to be the reduction of Ag⁺/Ag⁰ (reaction (c)),⁶⁷ further evidence of the successful synthesis of Mn-BTC@Ag₅[BW₁₂O₄₀]. It is noteworthy that the CV curve area of Mn-BTC@Ag₅[BW₁₂O₄₀]-NF in the figure is obviously larger than those of the other two electrodes. The above data show that the Mn-BTC@Ag₅[BW₁₂O₄₀]-NF has higher capacitance.

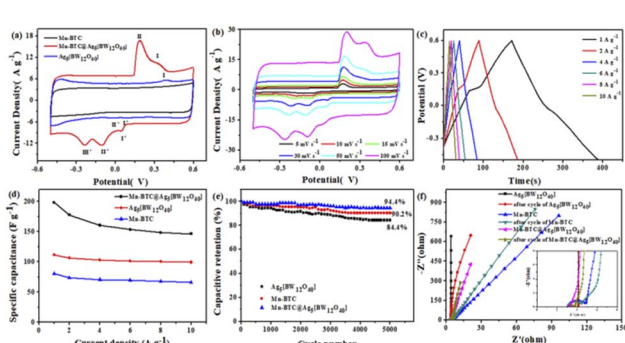
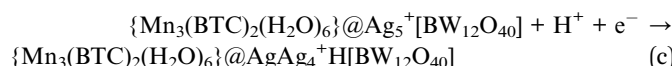
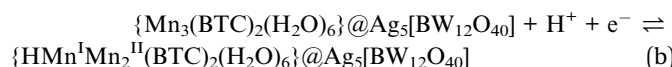


Fig. 4 (a) The CVs at 50 mV s⁻¹ scan rate; (b) the CVs at diverse scan rates for Mn-BTC@Ag₅[BW₁₂O₄₀]-NF, and (c) GCD curves of different current densities for Mn-BTC@Ag₅[BW₁₂O₄₀]-NF; (d) specific capacitance at diverse current densities; (e) 5000 cycles, and (f) EIS before and after 5000 cycles of the three compounds.

As can be seen from Fig. 4b, the CV curves of Mn-BTC@Ag₅[BW₁₂O₄₀]-NF at diverse scanning speeds show that all CV curves are similar in shape. With a scanning speed of up to 100 mV s⁻¹, the redox peaks observed were the same, indicating that it has good kinetic reversibility.⁶⁸ With the enhancement of scanning speed, the oxidation peaks and reduction peaks move to a positive potential and negative potential, respectively, indicating that electrode polarization will occur with the enhancement of the scanning rate. Moreover, the CV curve area augments gradually with the enhancement of scanning speed, indicating that Mn-BTC@Ag₅[BW₁₂O₄₀]-NF has a large capacitance. The CV curves of Ag₅[BW₁₂O₄₀]-NF and Mn-BTC-NF at diverse scan rates are shown in Fig. S6 and S7.[†]

As can be seen from Fig. 4c, the GCD curves of Mn-BTC@Ag₅[BW₁₂O₄₀]-NF under diverse current densities show that the GCD curve area decreases with the enhancement of current density in the charge-discharge course. According to eqn (S1),[†] the specific capacitance of Mn-BTC@Ag₅[BW₁₂O₄₀]-NF is 198.09 F g⁻¹ at a current density of 1 A g⁻¹, which is larger than those of Mn-BTC-NF (80.6 F g⁻¹), Ag₅[BW₁₂O₄₀]-NF (110.6 F g⁻¹) and those in the literature, see Table S1.[†] The Faraday reaction is insufficient at higher current density, resulting in a significant reduction in Mn-BTC@Ag₅[BW₁₂O₄₀]-NF capacitance as current density augments. And the capacitance of Mn-BTC@Ag₅[BW₁₂O₄₀]-NF remains at 146.36 F g⁻¹ at 10 A g⁻¹, which is still 73.89% of the original capacity (Fig. 4d). The results show that Mn-BTC@Ag₅[BW₁₂O₄₀]-NF has excellent energy storage capacity and rate reversibility. In addition, Mn-BTC@Ag₅[BW₁₂O₄₀]-NF maintained good stability after 5000 cycles, and the capacitance retention was 94.4%, which was higher than those of the other two compounds (Fig. 4e).

In Fig. 4f, the EIS plots of Mn-BTC@Ag₅[BW₁₂O₄₀], Ag₅[BW₁₂O₄₀], and Mn-BTC are measured before and after the cycle are shown. The EIS curve can be viewed as two parts, with a high frequency range and a low frequency range, respectively. While the semicircular arc in the high frequency region is due to redox reactions on the electrode/electrolyte interface, the diagonal of the low frequency region corresponds to the diffusion of ions through the electrode. The R_s stands for solution resistance in an electrochemical system. It can be seen that Mn-BTC@Ag₅[BW₁₂O₄₀] has the smallest circle radius at high frequency, which confirms that it has great ionic conductivity, lower electrode interfacial ohmic resistance and faster redox electron transfer kinetics.⁶⁹ In addition, Mn-BTC@Ag₅[BW₁₂O₄₀] has a high slope in the low frequency range, indicating that its diffusion resistance is small. What's more, the R_s values of Mn-BTC@Ag₅[BW₁₂O₄₀] before and after cycles respectively are 2.89 Ω and 3.01 Ω with little change, indicating that it has excellent conductivity and high capacitance and is a good material for supercapacitors. Mn-BTC@Ag₅[BW₁₂O₄₀] has low resistance and good cycle stability, probably due to the introduction of the transition metal Mn²⁺, which has good electronic conductivity.

For further research on the value of Mn-BTC@Ag₅[BW₁₂O₄₀] as an electrode material for supercapacitors in practical application, with nickel foam as a collector and using 1 M Na₂SO₄



electrolyte solution, a symmetric supercapacitor (SSC) was prepared with Mn–BTC@Ag₅[BW₁₂O₄₀]. Fig. S8† shows a simulation of a symmetric SSC system. The CV curves at a scanning speed of 5–100 mV s^{−1} in the 0–1.0 V voltage window are shown in Fig. S8.† Along with the increase of the sweep rate, the area of the CV curves also magnifies, and the graphs are generally the same with good symmetry. Its GCD curves at a current density of 1–5 A g^{−1} are shown (Fig. 5a). During the charging process, the electrolyte ion is embedded inside the electrode, and an electrochemical double layer is formed between the electrolyte and the electrode. The discharge process is when the electrolyte ion embedded in the electrode moves back into the electrolyte solution. The change in specific capacitance is related to the efficiency involved when the electrolyte ions are embedded in the electrode material.⁷⁰ At the low current density, the electrolyte ions are fully embedded inside the electrode. As the current density increases, the contact between the ions and the electrode decreases, and the specific capacitance also decreases. According to eqn (S2),† the specific capacitance is 78.2 F g^{−1} at a current density of 1 A g^{−1}. At this current density, the energy density and power density are 10.9 W h kg^{−1} and 503.1 W kg^{−1} (according to eqn (S3) and (S4)†), higher than most of the reported ones (Fig. 5b).^{71–78} When the current density is 10 A g^{−1}, the capacitance retention rate is 92.9% after 5000 cycles (Fig. 5c). The electrochemical impedance (EIS) is evaluated so that we can better know the charge transfer rate. The R_s values of the nanomaterial before and after circulation are 18.56 and 19.37 Ω. A small change in resistance indicates great stability and a rapid charge transfer rate (Fig. 5d). Overall, the electrochemical performance is good.

3.3. Photocatalytic properties

Photocatalytic oxidation technology can completely decompose the toxic and refractory organic pollutants into ore-forming materials, so the photocatalytic degradation of organic dyes has attracted the attention of researchers.^{79–82} Studies have found that POMs have a high activity in photocatalytic degradation⁸³ and the advantages of being green and safe. MOFs have a wide

range of photocatalytic applications due to their abundant catalytically active sites.⁸⁴ Based on the above considerations, using Mn–BTC@Ag₅[BW₁₂O₄₀], Mn–BTC, and Ag₅[BW₁₂O₄₀] as catalysts, the degradation of RhB, MB, and MO was tested under ultraviolet irradiation. Fig. S10† shows the adsorption–desorption curve of the organic dyes by the three compounds under light avoidance conditions. It can be seen that the adsorption of the organic dye by each of the three compounds within 30 min increased with increasing time, and the adsorption amount did not change after 30 min, indicating that all the three compounds reached the absorption and detachment equilibrium after 30 min. According to formula 1 – C_t/C_0 (C_0 and C_t express the concentration of photocatalytic degradation or absorption of dyes at times 0 and t, respectively), it can be seen that Mn–BTC@Ag₅[BW₁₂O₄₀] (RhB 2.65%, MO 3.52%, and MB 2.25%), Mn–BTC (RhB 5.86%, MO 4.04%, and MB 3.74%), and Ag₅[BW₁₂O₄₀] (RhB 3.78%, MO 3.61%, and MB 3.76%) have weak light absorption properties and little adsorption to organic dyes. The photocatalytic degradation properties of the three compounds were then tested separately. As can be seen from Fig. 6a–c, the degradation efficiency of the three dyes did no longer change 140 min later. Without the addition of a catalyst, the photocatalytic degradation speeds of RhB, MB, and MO are 1.7%, 2.1%, and 2.5%, respectively (see Fig. S11†). Fig. S12 and S13† show the photocatalytic degradation profiles for organic dyes of Ag₅[BW₁₂O₄₀] (RhB 39.26%, MO 37.38%, and MB 32.26%) and Mn–BTC (RhB 25.87%, MO 33.33%, and MB 24.27%). The degradation rates of Mn–BTC@Ag₅[BW₁₂O₄₀] for the three dyes of MB, RhB, and MO are 95.6%, 94.1% and 90.7%, respectively, which are higher than those of Ag₅[BW₁₂O₄₀] and Mn–BTC. These results indicate that the synergistic interaction between the core and shell is beneficial for enhancing the photocatalytic performance of the compound, so that Mn–BTC@Ag₅[BW₁₂O₄₀] has a significant catalytic effect. In order to know the stability of the nanomaterial in the first photocatalysis was used for five photocatalytic cycles for three dyes (Fig. 6d–f). The residuary concentration (C_t/C_0) was almost unchanged after five cycles. The IR of the nanomaterial after five cycles was almost the same as before (see Fig. S14†). The results show that Mn–

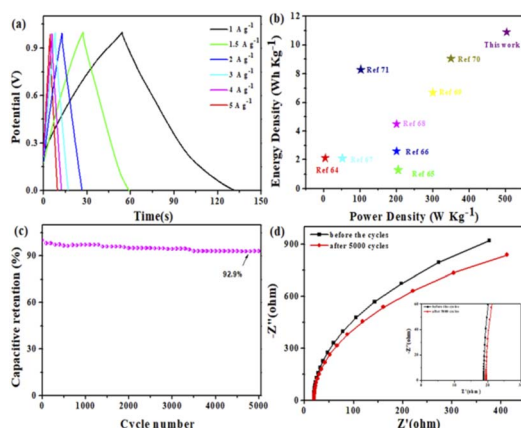


Fig. 5 (a) GCD curves, (b) the Ragone plot, (c) 5000 cycles and (d) EIS before and after 5000 cycles of the SSC.

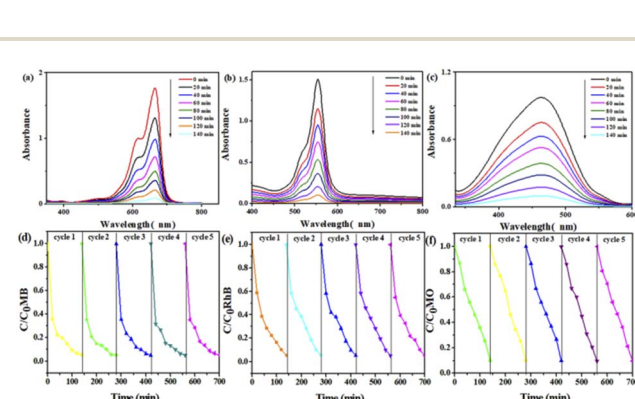


Fig. 6 UV absorption spectra of (a) MB, (b) RhB, and (c) MO organic dyes by photodegradation; the degradation effects toward (d) RhB, (e) MB, and (f) MO organic dyes for 5 recycles.



$\text{BTC@Ag}_5[\text{BW}_{12}\text{O}_{40}]$ has stable photocatalytic performance and good application potential.

To research the mechanism of photocatalytic degradation of dyes, photoluminescence (PL) spectroscopy and free radical capture experiments were performed. PL has been widely used to study the electron–hole composite probability to explore the photocatalytic properties of catalysts. According to the theory, it is generally believed that the lower the emission peak intensity, the lower the electron–hole composite probability, indicating that if the photogenerated charge has a longer lifetime, the photocatalysis would be better.⁸⁵ Fig. 7a shows that three compounds were subjected to the PL test at an excitation wavelength of 325 nm, and it shows that $\text{Mn-BTC@Ag}_5[\text{BW}_{12}\text{O}_{40}]$ has the lowest emission peak intensity, indicating a low electron–hole composite probability and theoretically better photocatalysis, consistent with the photocatalytic degradation dye results. Benzoquinone (BQ), isopropyl alcohol (IPA) and ethylenediaminetetraacetic acid (EDTA) were added to the three dyes as masking agents to mask superoxide radicals ($\cdot\text{O}_2^-$), hydroxyl radicals ($\cdot\text{OH}$), and holes (h^+), respectively. As can be seen from Fig. 7b, the degradation speed of the dyes reduced slightly after adding BQ and EDTA, proving that $\cdot\text{O}_2^-$ and h^+ aren't the decisive active intermediates. After adding IPA, the degradation rates of the dyes decreased significantly, and the degradation rates were as low as 23.32% (RhB), 24.51% (MO) and 55.3% (MB), respectively, indicating that $\cdot\text{OH}$ played a dominant role in this reaction, which is consistent with results in the literature.^{40,43}

Furthermore, the speculated mechanism of photocatalytic degradation of dyes is as follows from Fig. 8: under ultraviolet radiation, photogenerated electrons (e^-) move away from the valence band (VB) and move to the conduction band (CB), and they produce holes (h^+) on the VB (reaction (1)).⁸⁶ And h^+ can move from the VB of Mn-BTC to the VB of $\{\text{BW}_{12}\}$ and get adsorbed on the surface of $\{\text{BW}_{12}\}$ in large quantities. Moreover, h^+ can be easily captured by H_2O and generate $\cdot\text{OH}$ on the surface of the catalyst (reaction (2)).⁸⁷ The CB negative potential of Mn-BTC is larger than that of $\{\text{BW}_{12}\}$, so the electrons in the CB of $\{\text{BW}_{12}\}$ transfer to the CB of Mn-BTC, and the electrons react with O_2 dissolved in water to form $\cdot\text{O}_2^-$ (reaction (3)).⁸⁸ $\cdot\text{OH}$, as a strong oxidant, will spontaneously degrade the surrounding organic dye, eventually forming H_2O and CO_2 (reaction (4)).⁸⁹ The synergistic effect between the core–shell structure of $\text{Mn-BTC@Ag}_5[\text{BW}_{12}\text{O}_{40}]$ can promote e^- transfer

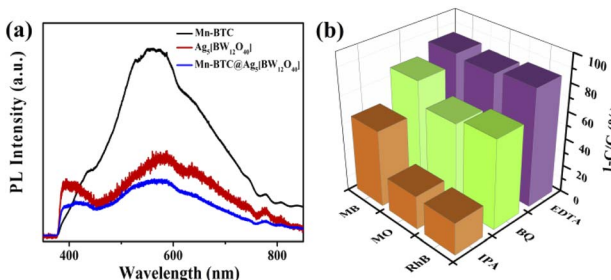


Fig. 7 (a) PL spectra of the three compounds; the (b) effect of masking agents (IPA, BQ, and EDTA) on MO, MB, and RhB degradation rates.

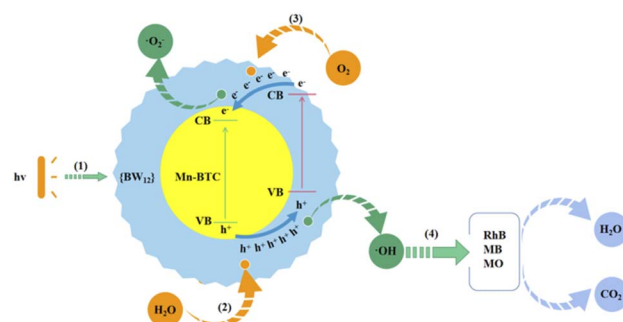


Fig. 8 The degradation mechanism of $\text{Mn-BTC@Ag}_5[\text{BW}_{12}\text{O}_{40}]$.

and the effective segregation of e^- – h^+ pairs and extends the service life of the carrier, which is the crucial factor to enhance photocatalytic activity.⁸⁶ And valence electrons of Mn generate new energy levels and split energy levels, which will shorten the electron transition time and also improve the photocatalytic reaction activity effectively.⁹⁰

4. Conclusions

In summary, $\text{Mn-BTC@Ag}_5[\text{BW}_{12}\text{O}_{40}]$ with a core–shell structure was triumphantly compounded though a simple grinding method and was successfully synthesized and directly used as a supercapacitor and photocatalyst. In the three-electrode system, the capacitance of the $\text{Mn-BTC@Ag}_5[\text{BW}_{12}\text{O}_{40}]$ electrode is 198.09 F g^{-1} at a current density of 1 A g^{-1} , which is larger than those of $\text{Ag}_5[\text{BW}_{12}\text{O}_{40}]$ (110.6 F g^{-1}) and Mn-BTC (80.6 F g^{-1}). What's more, the preservation speed of the capacitance maintains 94.4% after 5000 cycles. In the symmetric SSC system, the power density, energy density, and specific capacitance of the symmetric supercapacitor are 503.1 W kg^{-1} , 10.9 W h kg^{-1} and 78.2 F g^{-1} . Meanwhile, capacitance preservation speed maintains 92.9% after 5000 cycles. Under ultraviolet radiation, $\text{Mn-BTC@Ag}_5[\text{BW}_{12}\text{O}_{40}]$ exhibits excellent photocatalytic degradation ability for typical dyes. Little change in the dye degradation rate occurred after five cycles. Therefore, the synthesized nanomaterials could be used for the development of satisfactory photocatalytic materials.

Author contributions

Caihong Shi: writing – original draft. Ning Kang: data curation. Chunmei Wang: visualization. Kai Yu: formal analysis. Jinghua Lv: methodology. Chunxiao Wang: validation. Baibin Zhou: visualization, conceptualization, and writing – review & editing.

Conflicts of interest

There are no conflicts to declare.

Acknowledgements

This work was supported by the National Natural Science Foundation of China (22171061 and 21771046), the 2020 Central Government's Plan to Support the Talent Training

Project of the Reform and Development Fund of Local Universities (1401120002), the Natural Science Foundation of Heilongjiang Province of China (ZD2021B002), and the Excellent Scientific Research Team Project of Harbin Normal University (XYKT2020001).

Notes and references

- Y. Zheng, J. Liu, J. Liang, M. Jaroniec and S. Z. Qiao, *Energy Environ. Sci.*, 2012, **5**, 6717–6731.
- X. Y. Chu, F. L. Meng, T. Deng and W. Zhang, *Nanoscale*, 2021, **13**, 5570–5593.
- S. Makino, Y. Yamauchi and W. Sugimoto, *J. Power Sources*, 2013, **227**, 153–160.
- J. Tang, R. R. Salunkhe, H. Zhang, V. Malgras, T. Ahamad, S. M. Alshehri, N. Kobayashi, S. Tominaka, Y. Ide and J. H. Kim, *Sci. Rep.*, 2016, **6**, 1–8.
- S. Chen, Y. F. Xiang, M. K. Banks, C. Peng, W. J. Xu and R. X. Wu, *Nanoscale*, 2018, **10**, 20043–20052.
- H. Y. Chen, R. Al-Oweini, J. Friedl, C. Y. Lee, L. L. Li, U. Kortz, U. Stimming and M. Srinivasan, *Nanoscale*, 2015, **7**, 7934–7941.
- X. H. Wang, F. Rong, F. F. Huang, P. He and Y. Yang, *J. Alloys Compd.*, 2019, **789**, 684–692.
- K. B. Wang, Z. K. Wang, S. Wang, Y. Chu, R. Xi, X. Y. Zhang and H. Wu, *Chem. Eng. J.*, 2019, **367**, 239–248.
- B. Akinwolemiwa, C. Wei and G. Z. Chen, *Electrochim. Acta*, 2017, **247**, 344–357.
- A. V. Anyushin, A. Kondinski and T. N. Parac-Vogt, *Chem. Soc. Rev.*, 2022, **49**, 382–432.
- G. N. Wang, T. T. Chen, C. J. Gómez-García, F. Zhang, M. Y. Zhang, H. Y. Ma, H. J. Pang, X. M. Wang and L. C. Tan, *Small*, 2020, **16**, 2001626–2001633.
- Y. Wang, Y. Y. Wang, L. Zhang, C. S. Liu and H. Pang, *Inorg. Chem. Front.*, 2019, **6**, 2514–2520.
- M. Yang, S. Rong, X. M. Wang, H. Y. Ma, H. J. Pang, L. C. Tan and Y. X. Jiang, *ChemNanoMat*, 2021, **7**, 299–306.
- N. I. Gumerova and A. Rompel, *Chem. Soc. Rev.*, 2020, **49**, 7568–7601.
- M. R. Horn, A. Singh, S. Alomari, S. Goberna-Ferrón, R. Benages-Vilau, N. Chodankar, N. Motta, K. Ostrikov, J. MacLeod, P. Sonar, P. Gomez-Romero and D. Dubal, *Energy Environ. Sci.*, 2021, **14**, 1652–1700.
- H. Y. Zhao, Y. Z. Li, J. W. Zhao, L. Wang and G. Y. Yang, *Coord. Chem. Rev.*, 2021, **443**, 213966–213985.
- D. Wang, L. Liu, J. Jiang, L. Chen and J. Zhao, *Nanoscale*, 2020, **12**, 5705–5718.
- W. Jia, J. L. Zhang, Z. J. Lu, S. Q. Wang and S. Z. Feng, *Nanoscale*, 2020, **12**, 3902–3906.
- M. L. Wang, Y. Zhang, T. Y. Zhang, Y. Li, M. Z. Cui, X. Cao, Y. Lu, D. D. Peng, W. F. Liu, X. G. Liu, T. Wang and Y. Z. Huang, *Nanoscale*, 2020, **12**, 11887–11898.
- A. J. Liu, F. Xu, S. D. Han, J. Pan and G. M. Wang, *Cryst. Growth Des.*, 2020, **20**(11), 7350–7355.
- A. Naim, Y. Chevalier, Y. Bouzidi, P. Gairola, P. Mialane, A. Dolbecq, F. Avenier and J. P. Mahy, *Inorg. Chem. Front.*, 2020, **7**, 2362–2369.
- C. T. Buru, P. Li, B. L. Mehdi, A. Dohnalkova, A. E. Platero-Prats, N. D. Browning, K. W. Chapman, J. T. Hupp and O. K. Farha, *Chem. Mater.*, 2017, **29**, 5174–5181.
- M. Samaniyan, M. Mirzaei, R. Khajavian, H. Eshtiagh-Hosseini and C. Streb, *ACS Catal.*, 2019, **9**, 10174–10191.
- J. H. Shi, H. X. Zhang, P. S. Wang, P. Wang, J. J. Zha, Y. Liu, J. Gautam, L. N. Zhang, Y. Wang, J. Xie, L. B. Ni, G. W. Diao and Y. G. Wei, *CrystEngComm*, 2021, **23**, 8482–8489.
- H. R. Chen, K. Shen, Q. Mao, J. Y. Chen and Y. W. Li, *ACS Catal.*, 2018, **8**, 1417–1426.
- H. Y. Jin, C. X. Guo, X. Liu, J. L. Liu, A. Vasileff, Y. Jiao, Y. Zheng and S. Z. Qiao, *Chem. Rev.*, 2018, **118**, 6337–6408.
- D. Yang and B. C. Gates, *ACS Catal.*, 2019, **9**, 1779–1798.
- S. F. Ma, J. Ying, Y. P. Zhang and A. X. Tian, *CrystEngComm*, 2022, **24**, 2891–2902.
- J. L. Zhuo, Y. L. Wang, Y. G. Wang, M. Q. Xu and J. Q. Sha, *CrystEngComm*, 2022, **24**, 579–586.
- X. Xu, Y. P. Zhang, J. Ying, L. Jin, A. X. Tian and X. L. Wang, *CrystEngComm*, 2022, **24**, 1267–1278.
- C. X. Sun, J. Ying, Y. P. Zhang, L. Jin, A. X. Tian and X. L. Wang, *CrystEngComm*, 2022, **24**, 587–600.
- C. Wang, S. Yao, Y. Chen, Z. Zhang and E. Wang, *RSC Adv.*, 2016, **6**, 99010–99015.
- C. Zhao, S. Li, H. Ma, C. Zhang, H. Pang, Y. Yu and Z. Zhang, *CrystEngComm*, 2016, **18**, 6233–6244.
- S. Wang, K. Yu, B. Wang, L. Wang, C. X. Wang, H. Zhang, C. M. Wang and B. B. Zhou, *New J. Chem.*, 2016, **40**, 7011–7017.
- K. Guo, X. Jiang, M. Xu, F. Li, S. Dong, Y. Zheng and L. Xu, *Chem. Commun.*, 2021, **57**, 11398–11401.
- Q. L. Liang, N. N. Du, L. G. Gong, C. X. Wang, C. M. Wang, K. Yu and B. B. Zhou, *New J. Chem.*, 2021, **45**, 14444–14450.
- W. J. Zhang, L. G. Gong, N. N. Du, C. X. Wang, K. Yu, C. M. Wang and B. B. Zhou, *Inorg. Chem.*, 2021, **60**, 16357–16369.
- S. J. Pang, L. G. Gong, N. N. Du, H. Luo, K. Yu, J. Q. Gao, Z. W. Zheng and B. B. Zhou, *Mater. Today Energy*, 2019, **13**, 239–248.
- X. Y. Zhao, L. G. Gong, C. X. Wang, C. M. Wang, K. Yu and B. B. Zhou, *Chem.-Eur. J.*, 2020, **26**, 4613–4619.
- L. Y. Wang, N. Kang, L. G. Gong, C. X. Wang, K. Yu, C. M. Wang and B. B. Zhou, *J. Energy Storage*, 2022, **46**, 103873.
- Z. W. Zheng, X. Y. Zhao, L. G. Gong, C. X. Wang, C. M. Wang, K. Yu and B. B. Zhou, *J. Solid State Chem.*, 2020, **288**, 121409.
- H. Liu, L. G. Gong, C. X. Wang, C. M. Wang, K. Yu and B. B. Zhou, *J. Mater. Chem. A*, 2021, **9**, 13161–13169.
- Y. Liang, N. Kang, C. M. Wang, K. Yu, J. H. Lv, C. X. Wang and B. B. Zhou, *Dalton Trans.*, 2022, **51**, 7613–7621.
- L. J. Xu, X. Y. Zhao, K. Yu, C. M. Wang, J. h. Lv, C. X. Wang and B. B. Zhou, *CrystEngComm*, 2022, **24**, 5614–5621.
- R. Mao, F. Y. Zhan, N. J. Bu, Y. L. Cao, P. F. Hu, G. D. Gong and Q. Zhen, *Mater. Lett.*, 2016, **173**, 111–114.
- X. H. Zhong, Y. Lu, F. Luo, Y. W. Liu, X. H. Li and S. X. Liu, *Chem.-Eur. J.*, 2018, **24**, 3045–3051.
- S. B. Li, L. Zhang, Y. Q. Lan, K. P. O. Halloran, H. Y. Ma and H. J. Peng, *Chem. Commun.*, 2018, **54**, 1964–1967.



48 P. F. Hu and Y. L. Cao, *Dalton Trans.*, 2012, **41**, 8908–8912.

49 A. M. Zhang, M. Zhang, D. Lan, H. N. Wang, Y. J. Tang, X. L. Wang, L. Z. Dong, L. Zhang, S. L. Li and Y. Q. Lan, *Inorg. Chem.*, 2018, **57**, 11726–11731.

50 Y. Benseghir, A. Lemarchand, M. Duguet, P. Mialane, M. Gomez-Mingot, C. Roch-Marchal, T. Pino, M. H. Ha-Thi, M. Haouas, M. Fontecave, A. Dolbecq, C. Sassoye and C. Mellot-Draznieks, *J. Am. Chem. Soc.*, 2020, **142**, 9428–9438.

51 S. Roy, V. Vemuri, S. Maiti, K. S. Manoj and U. Subbarao, *Inorg. Chem.*, 2018, **57**, 12078–12092.

52 C. Rocchiccioli-Deltcheff, M. Fournier, R. Franck and R. Thouvenot, *Inorg. Chem.*, 1983, **22**, 207–216.

53 N. N. Du, L. G. Gong, L. Y. Fan, K. Yu, H. Luo, S. J. Pang, J. Q. Gao, Z. W. Zheng, J. H. Lv and B. B. Zhou, *ACS Appl. Nano Mater.*, 2019, **2**, 3039–3049.

54 H. Lv, J. Song, Y. V. Geletii, J. W. Vickers, J. M. Sumliner, D. G. Musaev, P. Koegerler, P. K. Zhuk, J. Bacsa, G. Zhu and C. L. Hill, *J. Am. Chem. Soc.*, 2014, **136**, 9268–9271.

55 M. Bou, J. M. Martin and T. L. Mogne, *Appl. Surf. Sci.*, 1991, **47**, 149–161.

56 K. M. L. Taylor, W. J. Rieter and W. B. Lin, *J. Am. Chem. Soc.*, 2008, **130**, 14358–14359.

57 W. Luo, Z. H. Bao, W. H. Jiang, J. M. Liu, G. Feng, Y. Q. Xu, H. D. Tang and T. Wang, *Ceram. Int.*, 2019, **45**, 24750–24756.

58 Y. Wang, Y. Peng, L. N. Xiao, Y. Y. Hu, L. M. Wang, Z. M. Gao, T. G. Wang, F. Q. Wu, X. B. Cui and J. Q. Xu, *CrystEngComm*, 2012, **14**, 1049–1056.

59 J. W. Zhao, Y. P. Song, P. T. Ma, J. P. Wang and J. Y. Niu, *Solid State Chem.*, 2009, **182**, 1798–1805.

60 Y. L. Ren, D. D. Yang, N. Li and R. D. Huang, *Chin. J. Chem.*, 2017, **35**, 347–353.

61 Z. H. Yang, C. H. Ho and S. Lee, *Appl. Surf. Sci.*, 2015, **349**, 609–614.

62 J. G. Lv, R. Miao, M. Zhang, G. He, M. Zhao, B. Yu, W. Wang, B. Li and Z. Q. Sun, *J. Mater. Sci.: Mater. Electron.*, 2018, **29**, 16282–16288.

63 Y. M. Liang, N. Guo, L. L. Li, R. Q. Li, G. J. Ji and S. C. Gan, *New J. Chem.*, 2016, **40**, 1587–1594.

64 M. A. Stranick, *Surf. Sci. Spectra*, 1997, **6**, 47.

65 C. J. Wang, S. Yao, Y. Z. Chen, Z. M. Zhang and E. B. Wang, *RSC Adv.*, 2016, **6**, 99010–99015.

66 S. Maiti, A. Pramanik, U. Manju and S. Mahanty, *ACS Appl. Mater. Interfaces*, 2015, **7**, 16357–16363.

67 H. L. Zhu, Y. X. Tong and X. M. Chen, *J. Chem. Soc., Dalton Trans.*, 2000, 4182–4186.

68 G. J. Liang, X. L. Li, Y. B. Wang, S. Yang, Z. D. Huang, Q. Yang, D. h. Wang, B. B. Dong, M. S. Zhu and C. Y. Zhi, *Nano Research Energy*, 2022, **1**, e9120002.

69 X. H. Xiong, C. H. Yang, G. H. Wang, Y. W. Lin, X. Ou, J. H. Wang, B. T. Zhao, M. L. Liu, Z. Lin and K. V. Huang, *Energy Environ. Sci.*, 2017, **10**, 1757–1763.

70 X. C. Ye, Z. H. Lin, S. J. Liang, X. H. Huang, X. Y. Qiu, Y. C. Qiu, X. M. Liu, D. Xie, X. H. Xiong and H. Deng, *Nano Lett.*, 2019, **19**, 1860–1866.

71 A. M. White and R. C. T. Slade, *Synth. Met.*, 2003, **139**, 123–131.

72 M. Skunik, M. Chojak, I. A. Rutkowska and P. J. Kulesza, *Electrochim. Acta*, 2008, **53**, 3862–3869.

73 W. H. Li, K. Ding, H. R. Tian, M. S. Yao, B. Nath, W. H. Deng, Y. B. Wang and G. Xu, *Adv. Funct. Mater.*, 2017, **27**, 1702067–1702073.

74 D. Y. Fu, H. W. Li, X. M. Zhang, G. Y. Han, H. H. Zhou and Y. Z. Chang, *Mater. Chem. Phys.*, 2016, **179**, 166–173.

75 F. J. Miao, C. L. Shao, X. H. Li, K. X. Wang, N. Lu and Y. C. Liu, *J. Mater. Chem.*, 2016, **4**, 5623–5631.

76 S. H. Yang, Z. Z. Han, J. Sun, X. P. Yang, X. Hu, C. C. Li and B. Q. Cao, *Electrochim. Acta*, 2018, **268**, 20–26.

77 J. Wu, X. P. Zhang, F. X. Wei, Y. W. Sui and J. Q. Qi, *Mater. Lett.*, 2020, **258**, 126761.

78 Y. N. Li, D. P. Xu, M. M. Zhang, Q. Qin, M. Song, J. L. Zhou, Z. H. Chen, C. Teng and G. R. Ren, *J. Electroanal. Chem.*, 2021, **901**, 115781.

79 K. N. Li, S. S. Zhang, Y. H. Li, J. J. Fan and K. L. Lv, *Chin. J. Catal.*, 2021, **42**, 3–14.

80 H. Wang, W. X. Liu, X. He, P. Zhang, X. D. Zhang and Y. Xie, *J. Am. Chem. Soc.*, 2020, **142**, 14007–14022.

81 M. B. Wazir, M. Daud, F. Ali and M. A. Al-Harthi, *J. Mol. Liq.*, 2020, **315**, 113775–113819.

82 X. Zhang, J. Wang, X. X. Dong and Y. K. Lv, *Chemosphere*, 2020, **242**, 125144–125195.

83 J. Q. Gao, L. G. Gong, X. Y. Fan, K. Yu, Z. W. Zheng and B. B. Zhou, *ACS Appl. Nano Mater.*, 2020, **3**, 1497–1507.

84 J. Gu, Y. Peng, T. Zhou, J. Ma, H. Pang and Y. Yamauchi, *Nano Research Energy*, 2022, **1**, e9120009.

85 B. Wang, M. Y. Wang, F. Y. Liu, Q. Zhang, S. Yao, X. L. Liu and F. Huang, *Angew. Chem., Int. Ed.*, 2020, **59**, 1914–1918.

86 L. Yue, Y. Cao, Y. Han, Z. Li, X. Luo and Y. Liu, *J. Alloys Compd.*, 2021, **870**, 159339.

87 M. Ding, H. Yang, T. Yan, C. Wang, X. Deng, S. Zhang, J. Huang, M. Shao and X. Xu, *Nanoscale Res. Lett.*, 2018, **13**, 260.

88 H. Shen, X. Zhao, L. Duan, R. Liu, H. Wu, T. Hou, X. Jiang and H. Gao, *Appl. Surf. Sci.*, 2017, **391**, 627–634.

89 L. G. Gong, X. X. Qi, K. Yu, J. Q. Gao, B. B. Zho and G. Y. Yang, *J. Mater. Chem. A*, 2020, **8**, 5709–5720.

90 W. B. Zhang, Z. J. Zhang, S. W. Kwon, F. C. Zhang, B. Stephen, K. K. Kim, R. Jung, S. Kwon, K. Chung and W. Yang, *Appl. Catal., B*, 2017, **206**, 271–281.

